

Magnetic Fields in Stellar Jets

Patrick Hartigan¹, Adam Frank², Peggy Varnière², and Eric G. Blackman²

ABSTRACT

Although several lines of evidence suggest that jets from young stars are driven magnetically from accretion disks, existing observations of field strengths in the bow shocks of these flows imply that magnetic fields play only a minor role in the dynamics at these locations. To investigate this apparent discrepancy we performed numerical simulations of expanding magnetized jets with stochastically variable input velocities with the AstroBEAR MHD code. Because the magnetic field B is proportional to the density n within compression and rarefaction regions, the magnetic signal speed drops in rarefactions and increases in the compressed areas of velocity-variable flows. In contrast, $B \sim n^{0.5}$ for a steady-state conical flow with a toroidal field, so the Alfvén speed in that case is constant along the entire jet. The simulations show that the combined effects of shocks, rarefactions, and divergent flow cause magnetic fields to scale with density as an intermediate power $1 > p > 0.5$. Because $p > 0.5$, the Alfvén speed in rarefactions decreases on average as the jet propagates away from the star. This behavior is extremely important to the flow dynamics because it means that a typical Alfvén velocity in the jet close to the star is significantly larger than it is in the rarefactions ahead of bow shocks at larger distances, the one place where the field is a measurable quantity. Combining observations of the field in bow shocks with a scaling law $B \sim n^{0.85}$ allows us to infer field strengths close to the disk. We find that the observed values of weak fields at large distances are consistent with strong fields required to drive the observed mass loss close to the star. The increase of magnetic signal speed close to the star also means that typical velocity perturbations which form shocks at large distances will produce only magnetic waves close to the star. For a typical stellar jet the crossover point inside which velocity perturbations of $30 - 40 \text{ km s}^{-1}$ no longer produce shocks is $\sim 300 \text{ AU}$ from the source.

Subject headings: physical data and processes: MHD – physical data and processes: hydrodynamics – physical data and processes: shock waves – ISM: Herbig-Haro objects – ISM: jets and outflows

¹Dept. of Physics and Astronomy, Rice University, 6100 S. Main, Houston, TX 77005-1892, USA

²Dept. of Physics and Astronomy, University of Rochester, Rochester, NY 14627-0171

1. Introduction

Emission line images of star forming regions often reveal spectacular collimated, supersonic jets that emerge along the rotation axes of protostellar accretion disks (see Reipurth & Bally 2001; Ray et al. 2006, for reviews). The jets break up into knots which form multiple bow shocks as faster material overtakes slower material (e.g. Hartigan et al. 2001). Although measurements are scarce, when detected magnetic fields ahead of bow shocks are weak; hence, the dynamics of the bow shocks are controlled by velocity perturbations rather than by any magnetic instabilities. In these systems the magnetic field affects the flow mainly by reducing the compression in the dense postshock regions by adding magnetic pressure support (Morse et al. 1992, 1993).

However, close to the star there is evidence that magnetic fields may dominate the dynamics of jets. Strong observational correlations exist between accretion and outflow signatures (Cabrit et al. 1990; Hartigan et al. 1995), and most mechanisms for accelerating jets from disks involve magnetic fields (Ouyed & Pudritz 1997a; Casse & Ferreira 2000). Recent evidence for rotation in jets (Bacciotti et al. 2002; Coffey et al. 2004a) suggests that fields play an important role in jet dynamics, at least in the region where the disk accelerates the flow.

There has been considerable work done on the propagation of radiative jets with strong ($\beta \lesssim 1$) magnetic fields (Cerqueira & de Gouveia Dal Pino 1998; Frank et al. 1998, 1999; Frank et al. 2000; Gardiner et al. 2000; Gardiner & Frank 2000; O’Sullivan & Ray 2000; Stone & Hardee 2000; Cerqueira & de Gouveia dal Pino 1999; Cerqueira & de Gouveia Dal Pino 2001a,b; de Colle & Raga 2006). These studies have tended to explore how magnetic fields influence the large scale structure of jets, with the hope that the shape of jets may constrain the strength of the magnetic fields. These papers explored different field geometries, including ones connected to magneto-centrifugal launch models. Early studies focused on the development of nose-cones, which form when toroidal magnetic field is trapped due to pinch forces at the head of the flow. The role of toroidal fields acting as shock absorbers within internal working surfaces has also been explored by a number of authors. More recent studies have focused on the $H\alpha$ emission properties of MHD jets.

These papers did not, however, address the principle question of the current work, which is to link together measurements of the field strengths at different locations in real YSO jets and to infer the global run of the magnetic field and density with distance from the source. While earlier studies (Gardiner & Frank 2000; O’Sullivan & Ray 2000; Cerqueira & de Gouveia Dal Pino 2001a) did explicitly identify the crucial connection between internal working surfaces and magnetic field geometry when the initial field is helical, the effect this would have on the dependence of $B(\rho)$ and hence $B(r)$ in a velocity-variable flow was not considered, nor was

the possibility of a ‘magnetic zone’ close to the source where $v_{shock} \sim V_A$. The realization that such a region may have dynamically differentiable properties from the super-fast zones downstream is, to the best of our knowledge, new to this paper. Thus, the work we present here represents the first attempt to consider how the sparse magnetic fields measurements available in real YSO jets can be used to infer large scale field patterns in these objects.

In what follows we show that magnetically dominated outflows close to the disk are consistent with observations of hydrodynamically dominated jets at larger distances, provided the jets vary strongly enough in velocity to generate strong compressions and rarefactions. We begin by summarizing typical parameters of stellar jets, and then consider what these numbers imply for the MHD behavior of a jet as a function of its distance from the source for both the steady-state and time variable cases.

2. Observed Parameters of Stellar Jets

2.1. Velocity Perturbations

Stellar jets become visible as material passes through shock waves and radiates emission lines as it cools. Flow velocities, determined from Doppler motions and proper motions, are typically $\sim 300 \text{ km s}^{-1}$. The emission lines are characteristic of much lower shock velocities, $\sim 30 \text{ km s}^{-1}$ in most cases, leading to the idea that small velocity perturbations on the order of 10% of the flow speed (with occasional larger amplitudes as high as 50%) continually heat the jet (Reipurth & Bally 2001).

For jets like HH 111 which lie in the plane of the sky we can observe how the velocity varies at each point along the flow in real time by measuring proper motions of the emission. Thanks to the excellent spatial resolution of the Hubble Space Telescope, errors in these proper motions measurements are now only $\sim 5 \text{ km s}^{-1}$, which is low enough to discern real differences in the velocity of material in the jet. As predicted from emission line studies, the observed differences between adjacent knots of emission are typically $30 - 40 \text{ km s}^{-1}$ (Hartigan et al. 2001).

2.2. Density

Opening angles of stellar jets are fairly constant along the flow, ranging between a few degrees to $\gtrsim 20$ degrees (e.g. Reipurth & Bally 2001; Coffey et al. 2004b). Hence, to a good approximation we can take the flow to be conical. Once the jet has entered a strong working

surface it splatters to the sides, making its width appear larger, so the most reliable measures of jet widths are those close to the source. Other effects, such as precession of the jet and inhomogeneous ambient media also influence jet widths at large distances. In the absence of these effects, stellar jets can stay collimated for large distances because they are cool – the sound speeds of $\lesssim 10 \text{ km s}^{-1}$ are small compared with the flow speeds of several hundred km s^{-1} .

A well-known example of a conical flow is HH 34, which has a bright jet that has a nearly constant opening angle until it reaches a strong working surface (cf. Figure 6 of Reipurth et al. 2002). If we extend the opening angle defined by the sides of the jet close to the source to large enough distances to meet the large bow shock HH 34S, we find that the size of the jet at that distance is close to that inferred for the Mach disk of that working surface (Morse et al. 1992), as expected for a conical flow.

If jets emerge from a point then the density should be proportional to r^{-2} except perhaps within a few AU of the source where the wind is accelerated. New observations of jet widths range from a few AU at the source, to as high as 15 AU for bright jets like HH 30. For a finite source region of radius h , the density $n \sim (r + r_0)^{-2}$ for a conical flow, where $r_0 = h/\theta$, and θ is the half opening angle of the jet. For $h = 5 \text{ AU}$ and $\theta = 5 \text{ degrees}$, $r_0 = 57 \text{ AU}$.

For the purposes of constructing a set of fiducial values for jets, we adopt a density of 10^4 cm^{-3} at 1000 AU, and assume the width of the jet at the base to be 10 AU, with an opening half-angle of 5 degrees. These parameters produce a mass loss rate of $5 \times 10^{-8} \text{ M}_{\odot} \text{ yr}^{-1}$ for a flow velocity of 300 km s^{-1} . With these values we can calculate densities as a function of distance (the third column of Table 1). The fiducial values in the Table are only a rough guide to the densities observed in a typical jet. In addition to intrinsic variations between objects and density variations lateral to the jet, beyond $\sim 1000 \text{ AU}$ the observed densities increase substantially over a volume-averaged density in the Table owing to compression in the cooling zones of the postshock gas. Densities are correspondingly lower in the rarefaction regions between the shocks.

The density dependence in Table 1 for a conical flow appears about right from the data. New observations of the electron densities and ionization fractions at distances of $\sim 30 \text{ AU}$ of the jet in HN Tau indicate a total density between $\sim 2 \times 10^6 \text{ cm}^{-3}$ and 10^7 cm^{-3} (Hartigan et al. 2004), while the average density in jets such as HH 47, HH 111, and HH 34 at $\sim 10^4 \text{ AU}$ are $10^3 - 10^4 \text{ cm}^{-3}$ (Table 5 of Hartigan et al. 1994).

2.3. Magnetic Field

Because most stellar jets radiate only nebular emission lines, which are unpolarized and do not show any Zeeman splitting, measurements of magnetic fields in jets are not possible except for a few special cases. The only measurement of a field in a collimated flow close to the star appears to be that of Ray et al. (1997), who found strong circular polarization in radio continuum observations of T Tau S. The left-handed and right-handed circularly polarized light appear offset from one another some 10 AU on either side of the star, and the degree of polarization suggests a field of several Gauss. Ray et al. (1997) argue that the fields are too large to be attached to the star, and must come from compressed gas behind a shock in an outflow. However, Loinard et al. (2005) interpret the extended continuum emission from this object in terms of reconnection events at the star-disk interface. If the emission does arise in a jet, then even taking into account compression, the fields must be at least hundreds of mG in front of the shock to produce the observations.

One other technique has been successful in measuring magnetic fields in jets, albeit at larger distances. As gas cools by radiating behind a shock, the density, and hence the component of the magnetic field parallel to the plane of the shock (which is tied to the density by flux-freezing) increases to maintain the postshock region in approximate pressure equilibrium. As a result, the ratio of the magnetic pressure to the thermal pressure scales as T^{-2} (Hartigan 2003), so at some point in the cooling zone the magnetic pressure must become comparable to the thermal pressure even if the field was very weak in the preshock gas. The difference between the electron densities inferred from emission line ratios such as [S II] 6716/6731 for a nonmagnetic and weakly-magnetized shock can be as large as two orders of magnitude. Hence, one can easily measure the component of the magnetic field in the plane of the shock by simply observing the [S II] line ratio, provided the preshock density and the shock velocity are known from other data.

The total luminosity in an emission line constrains the preshock density well, so the problem comes down to estimating the shock velocity. For most jets this is a difficult task from line ratios alone because spectra from shocks with large fields and high shock velocities resemble those from small fields and low shock velocities (Hartigan et al. 1994). The easiest way to break this degeneracy is if the shock is shaped like a bow and the velocity is large enough that there is [O III] emission at the apex. Emission lines of [O III] are relatively independent of the field, and occur only when the shock velocity exceeds about 90 km s^{-1} . Hence, by observing how far [O III] extends away from the apex of the bow, and observing the shape of the bow, one can infer the shock velocity. Combining the shock velocity, the preshock density and the observed density in the cooling zone gives the magnetic field.

Unfortunately, only a few bow shocks have high enough velocities to emit [O III], so only

HH 34S and HH 111V have measured fields. The two cases yield remarkably similar results. In HH 34S, located 5.1×10^4 AU from the source, the preshock gas has a density of 65 cm^{-3} and a magnetic field of $10 \mu\text{G}$ (Morse et al. 1992), while HH 111V is 6.4×10^4 AU from the star and has a preshock density of 200 cm^{-3} and a magnetic field of $30 \mu\text{G}$ (Morse et al. 1993).

The ratio of B/n is the same for both HH 34S and HH 111V – we take $15 \mu\text{G}$ at a density of 100 cm^{-3} as a typical value. To fill in the field strengths throughout the table requires a relationship between B and n , which we now explore.

3. The Scaling Law $B \sim n^p$

There are two analytical scaling laws between the magnetic field and the density that might apply to stellar jets. If jets are driven by some sort of disk wind, then at distances beyond the Alfvén radius (typically a few AU, Anderson et al. 2005), the field will be mostly toroidal, and should decline as r^{-1} along the axis of the jet, where r is the distance from a point in the jet to the source. This radial dependence can be visualized by taking a narrow slice of thickness dz perpendicular to the axis of the jet. As the slice moves down the jet, its thickness remains constant because the jet velocity is constant at large distances from the disk, and the diameter of the slice increases linearly with the distance from the source as the flow moves. Hence the cross sectional area of the slice increases linearly with distance. The toroidal field strength, proportional to the number of field lines per unit area in the slice, must therefore scale as r^{-1} . A similar argument shows that the radial B scales as r^{-2} for a conical flow, which is why the toroidal field dominates in the jet outside of the region near the disk. For a conical flow, the density drops as r^{-2} , so $B \sim n^{0.5}$ for a steady flow. In contrast, if shocks and rarefactions dominate the dynamics, then the field is tied to the density, so $B \sim n$.

To determine which of these dependencies dominates we simulated an expanding magnetized flow that produces shock waves from velocity variability. Our simulations are carried out in 2.5D using the AstroBEAR adaptive mesh refinement (AMR) code. AMR allows high resolution to be achieved only in those regions which require it due to the presence of steep gradients in critical quantities such as gas density. AstroBEAR has been well-tested on variety of problems in 1, 2, 2.5D (Varniere et al. 2006) and 3D (Lebedev et al. 2004). Here we use the MHD version of the code in cylindrical symmetry (R, z) with $\mathbf{B} = B_\phi \mathbf{e}_\phi$, hence maintenance of $\nabla \cdot \mathbf{B} = 0$ is automatically achieved. We initialize our jet with magnetic field and gas pressure profiles ($B_\phi(R), P(R)$) which maintain cylindrical force equilibrium (Frank et al. 1998).

The spatial scale of the grid is arbitrary, but for plotting purposes we take it to be 10 AU so that the extent of the simulation resembles that of a typical stellar jet. Choosing a scale of 1 AU would match the dimensions at the base of the flow. The time steps are set to be 0.5 of the Courant-Friedrich-Levy condition, which is the smallest travel time for information across a cell in the simulation. For a 200 km s^{-1} jet and a 10 AU cell size this time interval is $\Delta t = 0.12$ years. The input jet velocity is a series of steps, whose velocity in km s^{-1} is given by $V = 200(1+fr)$, where f is the maximum amplitude of the velocity perturbation, and r is a random number between -1 and 1 . We ran simulations with $f = 0.5, 0.25,$ and 0.10 . We verified that a constant velocity jet gave a constant Alfvén velocity and $n \sim (r + r_0)^{-2}$ as predicted by analytical theory. The opening half angle of the jet was 5 degrees; a numerical run with a wider opening half angle of 15 degrees produced the same qualitative behavior as the more collimated models.

The first ten cells, taken to be the smallest AMR grid size, are kept at a fixed velocity V for the entire length of the pulse, and these ten cells are overwritten with a new random velocity after a pulse time of ~ 7.2 years ($60\Delta t$) for a grid size of 10 AU and a velocity of 200 km s^{-1} . Densities, velocities, and magnetic field strengths are mapped to a uniform spatial grid and printed out whenever the input velocity changes. Cooling is taken into account in an approximate manner by using a polytropic equation of state with index $\gamma = 1.1$. The density of the ambient medium is 1000 cm^{-3} and the initial density of the jet is held constant at 7500 cm^{-3} . We fixed the initial magnetic field to give a constant initial Alfvén speed of 35 km s^{-1} .

Figs. 1 – 4 show the results obtained for the $f = 0.5$ case. Similar plots were made for a single, nonmagnetic velocity perturbation in 1-D by Hartigan & Raymond (1993). Positive velocity perturbations form compression waves that steepen to form forward and reverse shocks (a bow shock and Mach disk in 2D), while negative velocity perturbations produce rarefactions as fast material runs ahead of slower material. The top panel in Fig. 1 shows the density along the axis of the jet once the leading bow shock has progressed off the grid. The strongest rarefactions, marked as open squares, follow closely to an r^{-2} law. Essentially once these strong rarefactions form in the flow, the gas there expands freely until it is overrun by a shock wave. Because each of the input velocity perturbations begins by forcing a velocity into the first 10 AMR zones (a region ~ 100 AU from the source depending on the size of the AMR zone), rarefactions caused by drops in the random velocity originate from $\log(r) \sim 2$ (Fig. 1). Hence, the open squares lie close to a line that goes through the steady-state solution at this point.

The bottom plot shows that shock waves and rarefactions dominate the flow dynamics. By the end of the simulation, the ~ 35 perturbations have interacted with one another,

colliding and merging to create only seven clear rarefactions and a similar number of shocks. The jet evolves quite differently than it would in steady state ($V_A = \text{constant}$). While the gas initially follows a $B \sim n^p$ law with $p = 0.5$, as soon as shocks and rarefactions begin to form, the value of p becomes closer to unity, with $p \sim 0.85$ a reasonable match to the entire simulation.

The important point is that once shock waves and rarefactions form, they will increase the value of p above that expected for a steady state flow. This increase means that the magnetic signal speed (a term that refers to fast magnetosonic waves, slow magnetosonic waves, or Alfvén waves, all of which have similar velocities because the sound speed is low, $\sim 10 \text{ km s}^{-1}$) drops overall at larger distances, especially within the rarefaction waves. Hence, small velocity perturbations that form only magnetic waves close to the star will generate shocks if they overrun rarefacted gas at large distances from the star. Essentially velocity perturbations redistribute the magnetic flux and thereby facilitate shock formation over much of the jet.

Using the numerical values from section 2.3, we can fill in the fourth column in Table 1 using $B/(15 \mu\text{G}) = (n/100 \text{ cm}^{-3})^{0.85}$. The fifth column of the Table gives the Alfvén speed in the preshock gas assuming full ionization, which is also appropriate for dynamics of partially ionized gas as discussed below.

4. Discussion

4.1. Evolution of a Typical Velocity Perturbation in an MHD Jet

Following how individual velocity perturbations evolve with time illustrates many of the dynamical processes that govern these flows. Fig. 2 shows a typical sequence of such perturbations, labeled A, B, C, D, and E, with initial velocities of 192, 230, 172, 223, and 295 km s^{-1} , respectively. In the left panel, which shows the simulation after 11 velocity pulses, a compression zone (marked as a solid vertical line) forms as B overtakes A, and both the density and Alfvén velocity V_A increase at this interface. Other compression zones grow from the interfaces of E/D and D/C. The rarefaction (dashed line) between B and C creates a characteristic ‘ramp’ profile in velocity, and at the center of this feature lies a broad, deep density trough an order of magnitude lower than the surrounding flow. The Alfvén speed in this trough has already dropped to nearly 10 km s^{-1} . For comparison, the steady state solution has $V_A = 35 \text{ km s}^{-1}$ everywhere, with a density that declines from the input value of 7500 cm^{-3} .

The right panel shows the simulation several hundred time steps later, after 12 velocity

pulses have passed through the input nozzle of the jet. Pulses A, B and C, have all evolved into something other than a step function, and little remains of pulse D, which will soon form the site of a merger between the denser knots at the D/E and C/D interfaces. The compression wave between A and B (1125 AU at left, and 1475 AU at right) has an interesting kink in its velocity profile. The two steep sides of this kink would become forward and reverse shocks if it were not for the fact that the Alfvén speed there remains high enough, $\sim 35 \text{ km s}^{-1}$, to inhibit the formation of a shock.

The left panel of Fig. 3 shows the same region of the jet several pulse times later. The only remaining pulse in this section of the jet is E, which has formed both a forward (bow) shock and a reverse (Mach disk) shock. The Alfvén speed at $\sim 2300 \text{ AU}$ ahead of the forward shock and at $\sim 2100 \text{ AU}$ behind the reverse shock are both only $10 - 20 \text{ km s}^{-1}$, so this gas shocks easily. Both the forward and reverse shocks have magnetosonic Mach numbers of $2 - 3$. The working surface between these shocks has a density of $\sim 3 \times 10^4 \text{ cm}^{-3}$, a factor of 4 increase over the initial jet density at the source and about two orders of magnitude higher than the surrounding gas. The Alfvén speed there is 120 km s^{-1} , having reached a maximum of 140 km s^{-1} when the shock first formed. Pulses A through C have merged to create a zone of nearly constant velocity from $2400 - 3400 \text{ AU}$. The density in this region is far from constant, however, with the density in the feature at 2900 AU a factor of 500 higher than its surroundings. This type of feature can cause problems in estimating mass loss rates, because it is a dense blob with substantial mass that is no longer being heated by shocks, and may therefore not appear in emission line images.

The right panel of Fig. 3 shows the working surface of knot E after 3 more pulse times. The velocity perturbation E has weakened to $\sim 30 \text{ km s}^{-1}$ but still forms a pair of shocks because the surrounding gas has an Alfvén speed of only 10 km s^{-1} . The magnetic pressure in the working surface is high enough to cause the region to expand, which lowers the density and the Alfvén speed. In the right panel the working surface is now 200 AU wide and the Alfvén speed has dropped to about 70 km s^{-1} . A new shock is just forming at 3900 AU as all the material on the left side of the plot with $V > 200 \text{ km s}^{-1}$ overtakes slower, but relatively dense gas from 3900 AU to 4400 AU .

The continuous creation and merging of shocks, rarefactions, and compression waves leads to some interesting and unexpected results. Because dense knots can have significant magnetic pressure support, when they collide they can ‘bounce’, as has been seen before in simulations of colliding magnetized clouds (Miniati et al. 1999). Evidence for splashback from such a collision is evident later in the simulation where the velocity at one point drops to 70 km s^{-1} , lower than any of the input velocities, which all lie between 100 km s^{-1} and 300 km s^{-1} .

Magnetically, the overall effect is to concentrate the field into a few dense areas, which then subsequently expand (see also Gardiner & Frank 2000). Fig. 4 shows the Alfvén speed at end of the simulation, by which time the leading bow shock has propagated off the right end of the grid. Though there are a few areas that have large Alfvén speeds, most of the gas in the jet has a significantly lower V_A than the steady-state solution does (solid line). The graph shows that, on average, magnetic fields tend to be more important dynamically close to the star.

Lower-amplitude simulations (Fig. 5) show similar qualitative behavior both in the formation and propagation of shocks and rarefactions, and in the dependency of B vs. n . As expected, fewer shocks and rarefactions form in the low-amplitude simulations and the results are closer to the steady-state solution ($p = 0.5$). In all cases, areas of high Alfvén velocity concentrate into a few shocked regions where the density is high, and most locations along the jet have lower Alfvén speeds than those of the steady state case.

4.2. The Hydrodynamic and Magnetic Zones

As noted in section 3 and in Figs. 4 and 5, because $B \sim n^p$ along the jet with $p > 0.5$, the Alfvén speed $V_A \sim$ increases, as the density rises. When $n \gtrsim 10^5 \text{ cm}^{-3}$, a typical velocity perturbation of 40 km s^{-1} will produce a magnetosonic wave rather than a shock. This variation of the average magnetic signal speed with density, and therefore with distance, implies that jets can behave hydrodynamically at large distances, and magnetically close to the star.

Far from the star, the densities are low and the dynamics are dominated by multiple bow shocks and rarefactions that form as faster material overtakes slower material. The magnetic field reduces the compression in the cooling zones behind the shocks and cushions any collisions between knots, but is otherwise unimportant in the dynamics. The fiducial values in Table 1 show that this hydrodynamic zone typically extends from infinity to within about 300 AU of the star ($\sim 1''$ for a typical source), so most emission line images of jets show gas in this zone. Alternatively, when the magnetic signal speed is greater than a typical velocity perturbation, the magnetic field inhibits the formation of a shock unless the perturbation is abnormally large. Figs. 4 and 5 show that the boundary between the magnetic and hydrodynamic zones is somewhat ill-defined: magnetic forces dominate wherever the field is high enough, as occurs in a few places in the simulations at large distances, for example, in the aftermath of the collision of two dense knots. However, statistically we expect magnetic fields to prevent typical velocity perturbations from forming shocks inside of ~ 300 AU.

A potential complication with the above picture is that fields may dampen small velocity perturbations in the magnetic zone before the perturbations ever reach the hydrodynamic zone where they are able to create shocks. How such perturbations behave depends to a large degree on how disk winds initially generate velocity perturbations in response to variable disk accretion rates. If the mass loss is highly clumpy, then plasmoids of dense magnetized gas may simply decouple from one another at the outset, produce rarefactions, and thereby reduce the magnetic signal speed enough to allow the first shocks to form. In addition, the geometry of the field will not remain toroidal if the flow becomes turbulent owing to fragmentation, precession, or interactions between clumps. When both toroidal and poloidal fields are present, velocity variability concentrates the toroidal fields into the dense shocked regions and the poloidal field into the rarefactions (Gardiner & Frank 2000). The magnetic signal speed in poloidally-dominated regions drops as the jet expands, facilitating the formation of shocks in these regions.

It might be possible to confirm the existence of stronger fields in knots close to the source with existing instrumentation. As described in section 2.3, by combining proper motion observations with emission line studies one can infer magnetic fields provided the velocity perturbations have large enough amplitudes.

4.3. Connection to the Disk

At distances closer to the disk than 10 AU, a conical flow with a finite width ($n \sim (r + r_0)^{-2}$) is not likely to model the jet well. For a disk wind, the field lines should curve inward until they intersect the disk at $\lesssim 1$ AU, while the field changes from being toroidal to mostly poloidal. We can use the scaling law between magnetic field strength and density derived above to see if the field strengths are roughly consistent with an MHD launching scenario. With $B \sim n^{0.85}$, the Alfvén velocity equals the jet speed, $\sim 300 \text{ km s}^{-1}$, when $n \sim 4 \times 10^7 \text{ cm}^{-3}$ and $B \sim 0.9 \text{ G}$. A moderately strong shock could then increase the field strength to a few Gauss, as observed by Ray et al. (1997). Taking the density proportional to r^{-2} within 10 AU gives $r = 2.5 \text{ AU}$ when $v = 300 \text{ km s}^{-1}$, the correct order of magnitude for the Alfvén radius of an MHD disk wind. The footpoint of the field line in the disk would be $\sim 0.4 \text{ AU}$ for a central star of one solar mass.

The observed correlation of accretion and outflow signatures, together with the existence of a few very strong bow shocks in some jets, suggests that sudden increases in the mass accretion rate through the disk produce episodes of high mass loss that form knots in jets as the material moves away from the star. Young stars occasionally exhibit large accretion events known as FU Ori and EX Ori outbursts (Hartmann et al. 2004; Briceño et al. 2004),

that may produce such knots. However, because knots typically take tens of years to move far enough away from the star to be spatially resolved, it has been difficult to tie an accretion event to a specific knot in a jet. In the case of a newly-ejected knot from the T Tauri star CW Tau, there does not appear to have been an accretion event at the time of ejection, though the photometric records are incomplete (Hartigan et al. 2004).

Because magnetic fields must dominate jets close to the disk, it is possible that the origin of jet knots is purely magnetic. Models of time-dependent MHD jets have produced knots that are purely magnetic in nature, and do not require accretion events Ouyed & Pudritz (1997b). For this scenario to work the mechanism of creating the knots must also impart velocity differences on the order of 10% of the flow velocity in order to be consistent with observations of velocity variability at large distances from the star. It may also be necessary to decouple the field from the gas via ambipolar diffusion in order to reduce the Alfvén speed enough to allow these velocity perturbations to initiate shocks and rarefactions. However, ambipolar diffusion timescales appear to be too long to operate efficiently in jet beams (Frank et al. 1999). One way to distinguish between accretion-driven knots and pure magnetic knots is to systematically monitor the brightness of T Tauri stars with bright forbidden lines over several decades to see whether or not accretion events are associated with knot ejections.

4.4. Effects of Partial Preionization

The ionization fraction of a gas affects how it responds to magnetic disturbances. Cooling zones of jets are mostly neutral – the observed ionization fractions of bright, dense jets range from $\sim 3\% - 7\%$ (Hartigan et al. 1994; Podio et al. 2006), and rise to $\sim 20\%$ for some objects (Bacciotti & Eisloffel 1999). The ionization fraction is higher close to star in some jets, $\sim 20\%$ if the emission comes from a shocked zone, and as much as 50% for a knot of uniform density (Hartigan et al. 2004), while in HH 30 the ionization fraction rises from a low value of $\lesssim 10\%$ to about 35% before declining again at larger distances (Hartigan & Morse 2007).

The Alfvén speed in a partially ionized gas like a stellar jet is inversely proportional to the density of ions, not to the total density. If the Alfvén speed exceeds the shock velocity, then ions accelerated ahead of the shock collide with neutrals and form a warm precursor there. If the precursor is strong enough it can smooth out the discontinuity of the flow variables at the shock front into a continuous rise of density and temperature known as a C-shock (Draine 1980; Draine et al. 1983). Precursors have been studied when the gas is molecular (Flower et al. 2003; Ciolek et al. 2004), but we have not found any calculations of

the effects precursors have on emission lines from shocks when the preshock gas is atomic and mostly neutral.

Dynamically the main issue is whether or not the magnetic signal speed in the preshock gas is large enough to inhibit the formation of a shock. Because ions couple to the neutrals in the precursor region via strong charge exchange reactions, any magnetic waves in this region should be quickly mass-loaded with neutrals. Hence, the relevant velocity for affecting the dynamics is the Alfvén velocity calculated from the total density, and not the density of the ionized portion of the flow. Another way to look at the problem is to consider the compression behind a magnetized shock, taking a large enough grid size so the precursor region is unresolved spatially. By conserving mass, momentum, and energy across the shock one finds that the compression in a magnetized shock varies with the fast magnetosonic Mach number in almost an identical way that the compression in a nonmagnetized shock varies with Mach number (Figure 1 of Hartigan 2003). Hence, the effective signal speed that determines the compression is calculated using the total density, and not the density of the ionized component. For this reason we use the total density to calculate the Alfvén speed in the fifth column of Table 1.

5. Summary

We have used observations of magnetic fields and densities in stellar jets at large distances from the star to infer densities and field strengths at all distances under the assumptions of a constant opening angle for the flow and flux-freezing of the field. Numerical simulations of variable MHD jets show that shocks and rarefactions dominate the relation between the density n and the magnetic field B , with the relation approximately $B \sim n^p$, with $1 > p > 0.5$. Because $p > 0.5$, the Alfvén velocity increases at higher densities, which occur on average closer to the star. This picture of a magnetically dominated jet close to the star that gives way to a weakly-magnetized flow at larger distances is consistent with existing observations of stellar jets that span three orders of magnitude in distance. Velocity perturbations effectively sweep up the magnetic flux into dense clumps, and the magnetic signal speed drops markedly in the rarefaction zones between the clumps, which allows shock waves to form easily there. For this reason, magnetic fields will have only modest dynamical effects on the visible bow shocks in jets, even if fields are dynamically important in a magnetic zone near the star.

This research was supported in part by a NASA grant from the Origins of Solar Systems Program to Rice University. We thank Sean Matt and Curt Michel for useful discussions on

the nature of magnetic flows.

REFERENCES

- Anderson, J., Li, Z-Y., Krasnopolsky, R., & Blandford, R. 2005, ApJ 590, L107
- Bacciotti, F. & Eisloffel, J. 1999, A&A 342, 717
- Bacciotti, F., Ray, T., Mundt, R., Eisloffel, J., & Solf, J. 2002, ApJ 576, 222
- Briceño, C., Vivas, A., Hernandez, J., Calvet, N., Hartmann, L., Megeath, T., Berlind, P., Calkins, M., & Hoyer, S. 2004, ApJ 606, L123
- Cabrit, S., Edwards, S., Strom, S., & Strom, K. 1990, ApJ 354, 687
- Casse F., & Ferreira, J. 2000, A&A 361, 1178
- Cerqueira, A. H., de Gouveia Dal Pino, E. M., & Herant, M. 1998, ApJ 489, L185
- Cerqueira, A. H., & de Gouveia dal Pino, E. M. 1999, ApJ 510, 828
- Cerqueira, A. H., & de Gouveia Dal Pino, E. M. 2001, ApJ 560, 779
- Cerqueira, A. H., & de Gouveia Dal Pino, E. M. 2001, ApJ 550, L91
- Ciolek, G., Roberge, W., & Mouschovias, T. 2004, ApJ 610, 781
- Coffey, D., Bacciotti, F., Woitas, J., Ray, T., & Eisloffel, J. 2004a, ApJ 604, 758
- Coffey, D., Downes, T., & Ray, T. 2004b, A&A 419, 593
- de Colle, F., & Raga, A. C. 2006, A&A 449, 1061
- de Gouveia dal Pino, E. M. 2005, AIP Conf. Proc. 784, Magnetic Fields in the Universe: From Laboratory and Stars to Primordial Structures, p183
- Draine, B. T. 1980, ApJ 241, 1021
- Draine, B. T., Roberge, W. G., & Dalgarno, A. 1983, ApJ 264, 485
- Flower, D., Le Bourlot, J., Pineau des Forets, G., & Cabrit, S. 2003, MNRAS 341, 70
- Frank, A., Ryu, D., Jones, T., & Noriega-Crespo, A. 1998, ApJ 494, L79
- Frank, A., Gardiner, T., Delemarter, G., Lery, T., & Betti, R. 1999, ApJ 524, 947
- Frank, A., Lery, T., Gardiner, T. A., Jones, T. W., & Ryu, D. 2000, ApJ 540, 342
- Gardiner, T., & Frank, A. 2000, ApJ 545, L153

- Gardiner, T. A., Frank, A., Jones, T. W., & Ryu, D. 2000, ApJ 530, 834
- Hartigan, P., Edwards, S., & Pierson, R. 2004, ApJ 609, 261
- Hartigan, P., Edwards, S., & Ghandour, L. 1995, ApJ 452, 736
- Hartigan, P., & Raymond, J. 1993, ApJ 409, 705
- Hartigan, P., & Morse, J. 2007, ApJ submitted
- Hartigan, P., Morse, J., & Raymond, J. 1994, ApJ 436, 125
- Hartigan, P., Morse, J., Reipurth, B., Heathcote, S. & Bally, J. 2001, ApJ 559, L157
- Hartigan, P. 2003, ApSS 287, 111
- Hartmann, L., Hinkle, K., & Calvet, N. 2004, ApJ 609, 906
- Lebedev, S., Ampleford, D., Ciardi, A., Bland, S., Chittenden, J., Haines, M., Frank, A., Blackman, E., & Cunningham, A. 2004, ApJ 616, 988
- Lery, T., & Frank, A. 2000, ApJ 533, 897
- Loinard, L., Mioduszewski, A., Rodriguez, L., Gonzalez, R., Rodriguez, M., & Torres, R. 2005, ApJ 619, L179
- Miniati, F., Ryu, D., Ferrara, A., & Jones, T. 1999, ApJ 510, 726
- Morse, J., Hartigan, P., Cecil, G., Raymond, J., & Heathcote, S. 1992, ApJ 399, 231
- Morse, J., Heathcote, S., Cecil, G., Hartigan, P., & Raymond, J. 1993, ApJ 410, 764
- O’Sullivan, S., & Ray, T. P. 2000, A&A 363, 355
- Ouyed, R., & Pudritz, R. 1997a, ApJ 482, 712
- Ouyed, R., & Pudritz, R. 1997b, ApJ 484, 794
- Podio et al. 2006, A&A, in press
- Ray, T., Dougados, C., Bacciotti, F., Eisloffel, J., & Chrysostomou, A. 2006, in *Protostars and Planets V*, B. Reipurth, D. Jewitt, & K. Keil eds., (Tucson:University of Arizona Press).
- Ray, T., Muxlow, T. W. B., Axon, D. J., Brown, A., Corcoran, D., Dyson, J., & Mundt, R. 1997, Nature 385, 415

Reipurth, B., Heathcote, S., Morse, J., Hartigan, P., & Bally, J. 2002, AJ 123, 362

Reipurth, B. & Bally, J. 2001, ARA&A 39, 403

Stone, J. M., & Hardee, P. E. 2000, ApJ 540, 192

Varniere, P., Poludnenko, A., Cunningham, A., Frank, A., & Mitran S, 2006, to appear in Springer's Lecture Notes in Computational Sciences and Engineering (LNCSE) series

Table 1.
Average Jet Parameters

Distance From Star (AU)	Arcseconds ^a	n (cm ⁻³) ^b	B _⊥	V _A (km s ⁻¹) ^c
10	0.02	2.5 × 10 ⁶	82 mG	113
30	0.06	1.5 × 10 ⁶	53 mG	94
100	0.2	4.5 × 10 ⁵	19 mG	62
300	0.6	8.8 × 10 ⁴	4.8 mG	35
10 ³	2.2	10 ⁴	0.75 mG	16
3 × 10 ³	6.5	1.2 × 10 ^{3d}	124 μG ^d	7.8
10 ⁴	22	110 ^d	16 μG ^d	3.3
3 × 10 ⁴	65	12 ^d	2.4 μG ^d	1.5

^aSpatial offset from the star at the distance of the Orion star forming region (460 pc).

^bDensities for a conical flow with a half opening angle of 5 degrees and a base width of 10 AU, taking the density to be 10⁴ cm⁻³ at 1000 AU.

^cThe Alfvén speed V_A determined from the total density n.

^dValues refer to an average density; densities at large distances are highly influenced by shocks and rarefaction waves, see text.

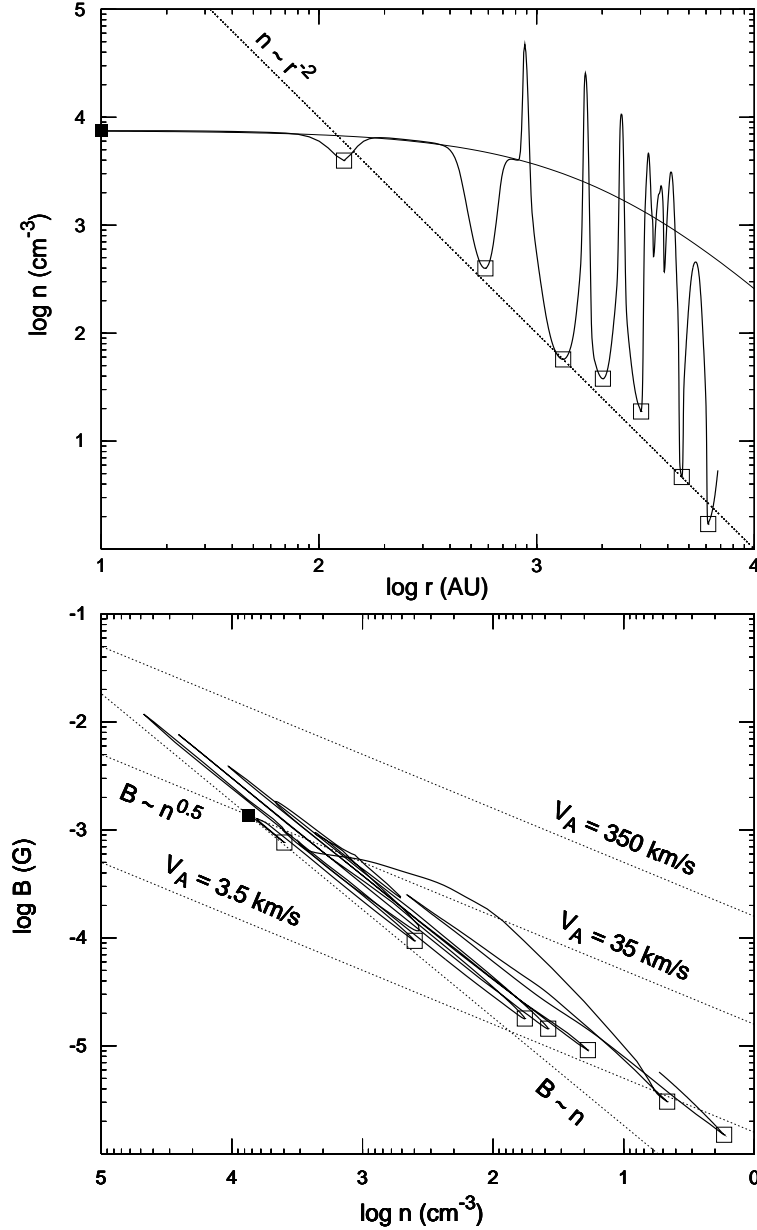


Fig. 1.— Top: A snapshot of the density vs. distance along the axis of an expanding, variable-velocity magnetized jet, taken once the first bow shock has left the grid to the right. The sharp peaks and valleys are shocks and rarefactions, respectively, that form as the flow evolves. Once strong rarefactions form they follow an approximate $n \sim r^{-2}$ law. The solid curve is the steady-state solution. Bottom: Same as top but for the magnetic field plotted vs. density. Shock waves move the curve to the upper left, and rarefactions drop it to the lower right. The locus of points along the flow follows an approximate power law, $B \sim n^p$, with $p \sim 0.85$. The simulation begins at the filled-in square, and the strongest rarefactions are denoted by open squares in both plots.

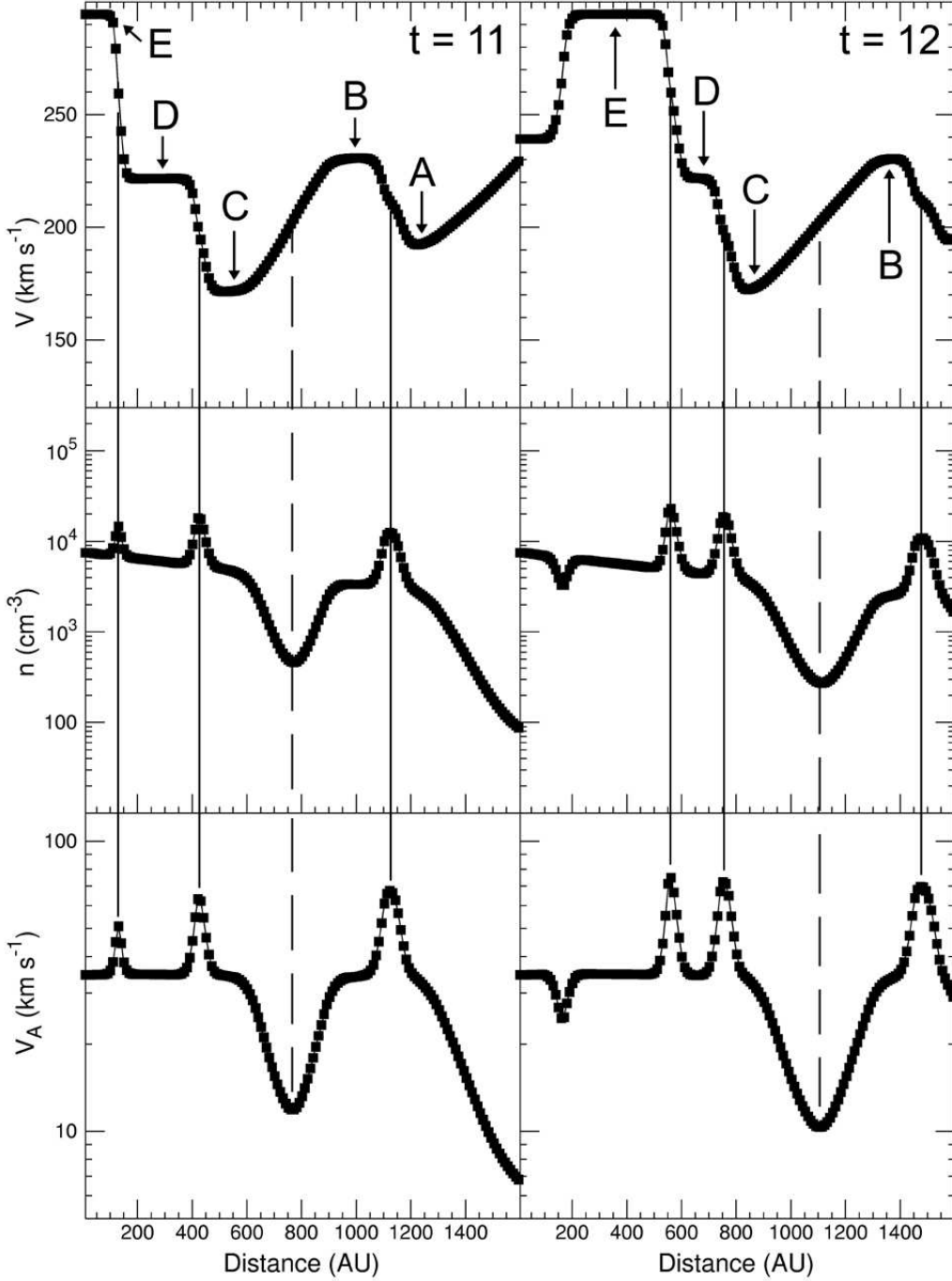


Fig. 2.— A typical sequence of velocity perturbations, labeled A – E. The top, middle, and bottom panels are the velocity, density, and Alfvén speed, respectively. Areas of compression are marked by solid vertical lines, and strong rarefactions by vertical dashed lines. The left and right panels show the first 1600 AU of the simulation at times that correspond to 11 and 12 input velocity pulses, respectively. The leading bow shock is located well to the right of the figures. In this, and subsequent figures the plots depict conditions along the axis of the jet. Further parameters of the simulation are discussed in the text.

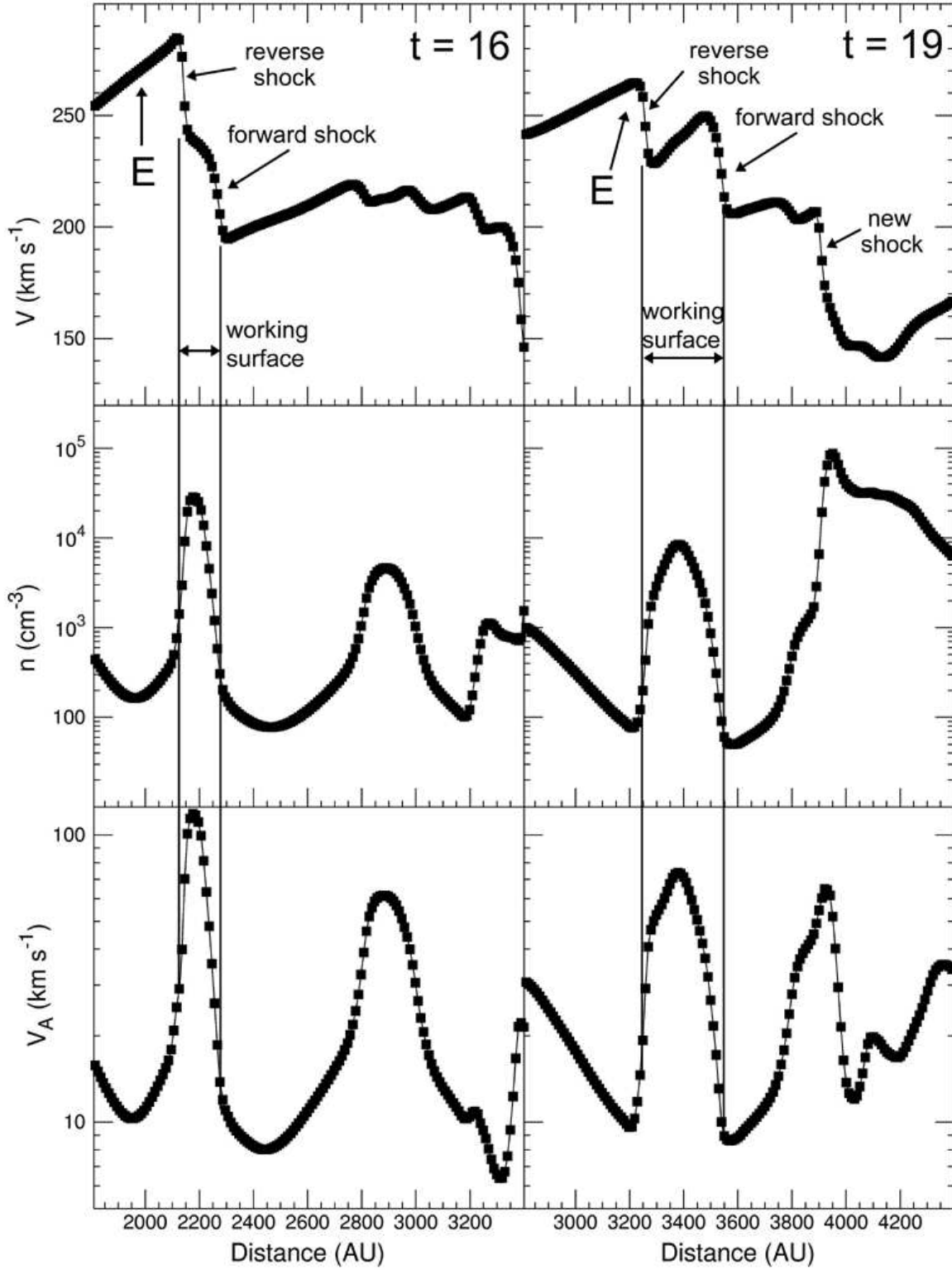


Fig. 3.— Same as Fig. 2 but at two later times. The evolution of the working surface of perturbation E is discussed in the text.

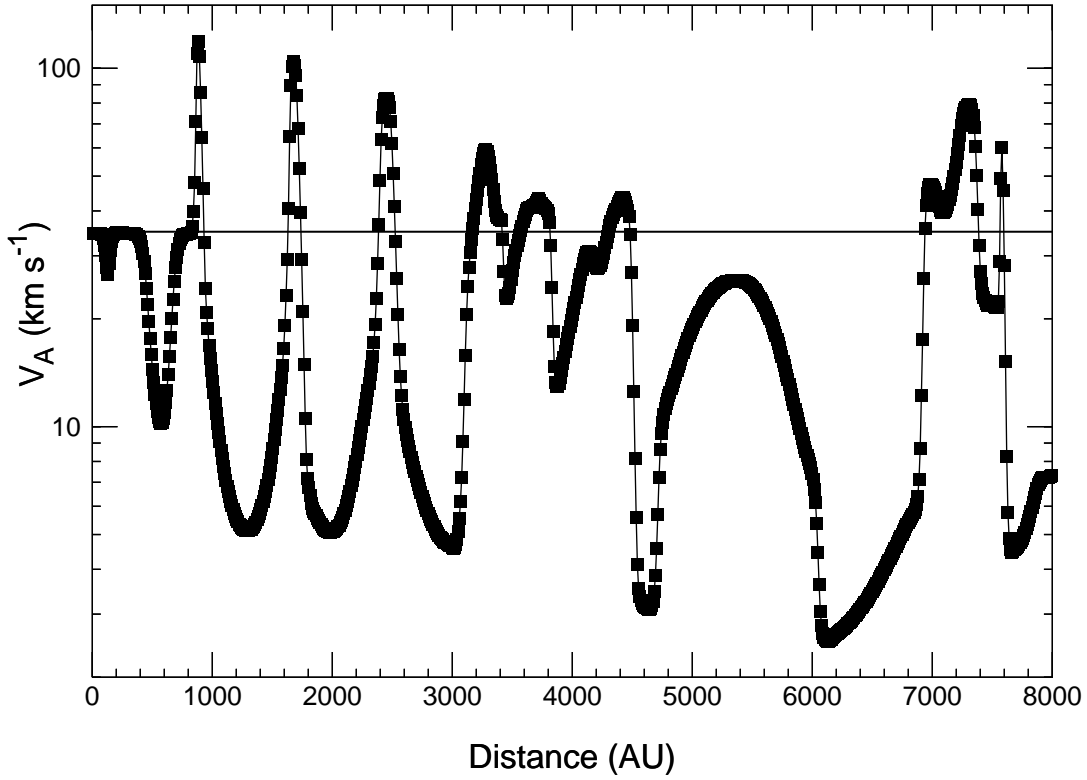


Fig. 4.— A plot of the Alfvén speed at the end of the simulation along the axis of the jet. The leading bow shock has propagated off the end of the grid. Magnetic flux concentrates into a few dense knots. Most points fall below the steady-state solution depicted as a solid line at 35 km s^{-1} .

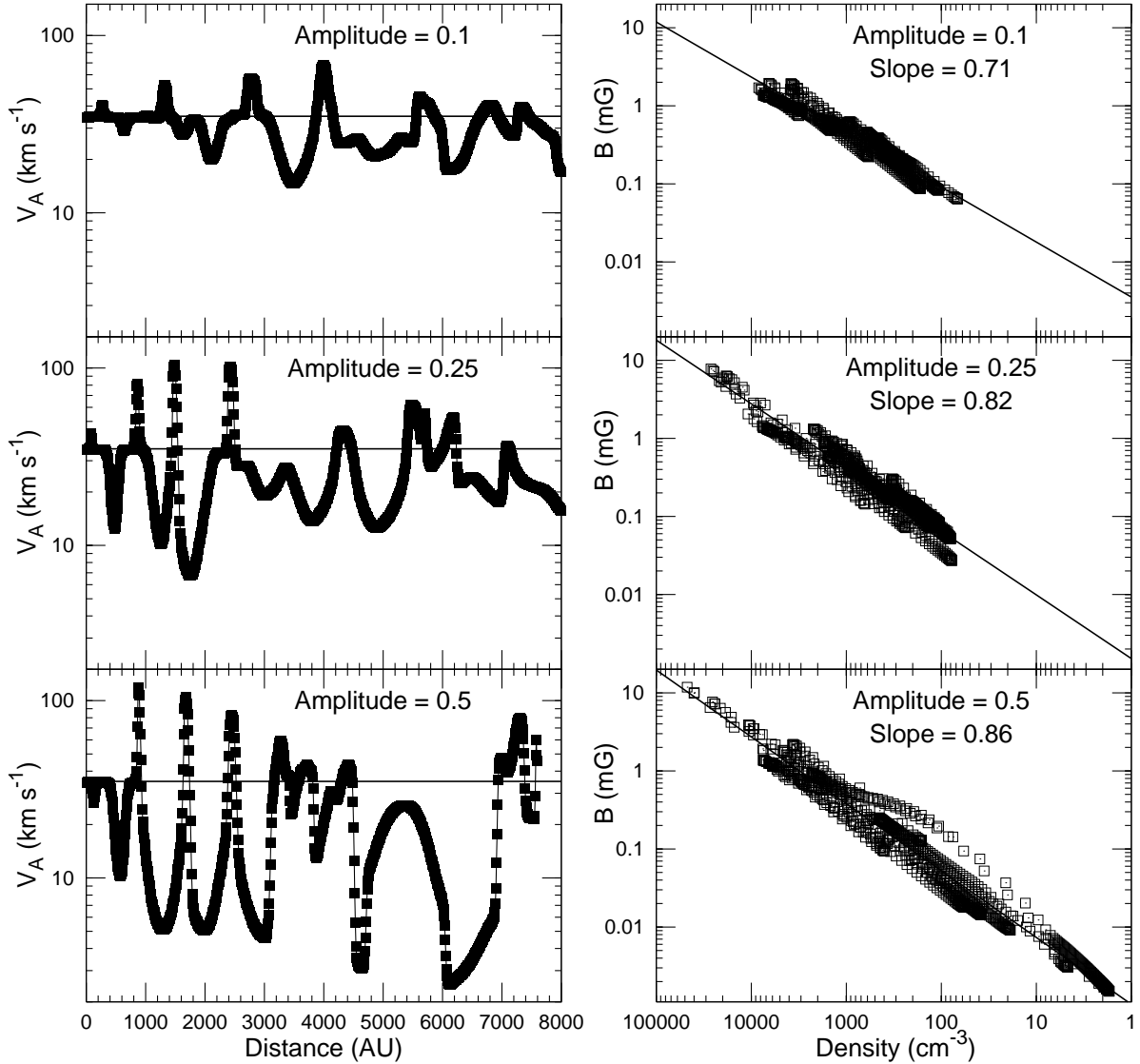


Fig. 5.— Left: Plots of the Alfvén speed V_A vs. distance for three different maximum perturbation amplitudes. The horizontal line marks $V_A = 35 \text{ km s}^{-1}$, which remains constant with distance when the input flow velocity does not vary. Lower-amplitude simulations have more modest compressions and rarefactions, but the effect of the perturbations in all cases is to concentrate high areas of V_A into a few cells, while a typical value of V_A declines with distance. Right: Analogous plots of the magnetic field B vs. density n show that $B \sim n^p$, with $0.5 < p < 1$. Higher amplitude perturbations produce correspondingly larger changes in both B and n .